Electronic Supplementary Information

Ti$_3$C$_2$T$_x$ MXene induces strong electronic metal-support interaction with Ni nanoparticles for hydrogen evolution reaction with Pt-like activity

Yixuan Han,[a] Xiaodan Yang,[a] Yidan Zhao,[a] Mingyang Zhao,[a] Hongming Sun,[*a] Jing Chen,[a] Jianchao Sun,[*b] Xiang Chen,[c] Cheng-Peng Li[*a]

[a] College of Chemistry, Tianjin Key Laboratory of Structure and Performance for Functional Molecules, Tianjin Normal University, Tianjin 300387, China
[b] School of Environment and Material Engineering, Yantai University, Yantai 264005, Shandong, China
[c] College of Textile Science and Engineering (International Institute of Silk), Zhejiang Sci-Tech University, Hangzhou 310018, China.

[*] Corresponding author. E-mail: hxxyshm@tjnu.edu.cn

Contents

1. Chemicals

2. Sample preparation

3. Characterizations

4. Electrocatalytic measurements

5. DFT Calculations

6. Figures and tables

References

1. Chemicals

LiF (99.99%), Ti_3AlC_2 (98%) and potassium thiocyanate (99%) were purchased from Shanghai Macklin Biochemical Co., Ltd. Nickel acetyl acetone (98%) , oleamine (80-90%), oleic acid (95%), potassium hydroxide (AR) and Pt/C (20%) were purchased from Meryer (Shanghai) Chemical Technology Co., Ltd. Triethylamine borane (97%) and hydrazine hydrate (98%) were purchased from Shanghai Aladdin Biochemical Technology Co., LTD. Graphene (AR) was purchased from Shenzhen Suiheng Technology Co., LTD. Hydrochloric acid (36-38%) and Nafion (D-521 dispersion 5% w/w in water & 1-propanol) were purchased from Alfa Aesar. Ar gas (99.99%) was purchased from Huanyu Co., Ltd.

2. Sample preparation

Synthesis of $Ti_3C_2T_x$ MXene

2 g LiF and 2 g Ti_3AlC_2 were slowly added into 20 mL of 9 M HCl solution, which was stirred at 45 °C for 72 h. The sample was centrifugally washed at 3500 rpm with distilled water to neutral. Increase the rotate speed to obtain less layers of $Ti_3C_2T_x$ MXene. Finally, $Ti_3C_2T_x$ MXene was dried in a vacuum oven at 65 °C.

Synthesis of $Ni/Ti_3C_2T_x$

80 mg $Ti_3C_2T_x$ MXene, 30 ml oleamine, 0.64 ml oleic acid and 0.7707 g $Ni(acac)_2$ were added into a 100 ml three-necked flask. This solution was heated to 110 °C in a vacuum, which was then filled with nitrogen and sealed. After dropping to 90 °C, 2.0 mL oleylamine with 0.7 mL triethylamine borane was injected into the above solution, which was heated at 90 °C for 1 h under stirring. After cooling to room temperature, the sample was washed by absolute ethanol, and dried in vacuum oven at 60 °C for 12 h. Then, the obtained $Ni/Ti_3C_2T_x$ precursor was calcined under a H_2/Ar mixture atmosphere for 2 h. The Ni/G hybrid was synthesized by this method except that graphene is used instead of MXene.

Synthesis of Ni

Firstly, 0.263 g $NiSO_4·6H_2O$ was dissolved in 10 mL of ice water. Subsequently, 94.5 mg $NaBH_4$ was added to the $NiSO_4$ solution and stirred in an ice bath for 2 h. Then, 1 mL (1 M) of KOH solution and 0.4 mL of $N_2H_4·H_2O$ were added this solution, which was transferred to a 25 mL autoclave, and heated at 150 °C for 4 h. After cooling to room temperature, the precipitation is centrifuged for several times and finally dried in a 60 °C vacuum oven.[1]

3. Characterizations

Powder XRD patterns were collected on a Rigaku model Ultima IV diffractometer with Cu-Kα X-ray, (20-60Kv) and a scanning speed of 5°/min. SEM images were performed on a FEI Nova Nano 230 scanning electron microscope. TEM equipped with EDS and SAED was taken on a Tecnai G2 F20 electron microscope and Kratos AXIS Ultra DLD energy dispersive spectrometer. The AFM images were taken with Bruker's proprietary ScanAsyst atomic force microscopy under scan mode (Bruker Dimension Icon). XPS was tested by Thermo Scientific K-Alpha spectrometer. The element composition was also evaluated by ICP-AES (PerkinElmer Optima 83000).

**4. Electrocatalytic measurements**

Electrochemical measurements were made in a three-electrode battery using a workstation double potentiostat (AFCBP1, Pine instrument) and Solartron ModuLab XM. The rotating disk electrode (RDE) with glassy carbon (PINE with disc area of 0.2471 cm^2), Hg/HgO electrode and carbon rod of glass carbon were used as working electrode, reference electrode and counter electrode, respectively. The 10 mg sample was ultrasonically dispersed in a mixture of 950 μL isopropyl alcohol and 50 μL Nafion and dropped on the surface of the RDE. Linear sweep voltammetry (LSV) plots were recorded in 1M KOH solution at a rate of 5 mV s^{-1}. Unless otherwise noted, all potentials are reported relative to the RHE scale. All polarization curves were iR-corrected according to $E_{iR} = E_{tested} - i \times 0.6\ R_s$ (R_s is the system resistance, E_{iR} is the corrected potential, and E_{tested} is the measured potential).

5. DFT Calculations

The Vienna Ab Initio Package (VASP) was used to make the DFT calculations within the generalized gradient approximation (GGA) by PBE formulation.[2,3] The projected augmented wave (PAW) potentials were applied to describe the ionic cores and take valence electrons into account using a plane wave basis set with a kinetic energy cutoff of 400 eV.[4] Partial occupancies of Kohn-Sham orbitals were allowed by using the Gaussian smearing method and a width of 0.05 eV. When energy change is $< 10^{-5}$ eV, the electronic energy is considered self-consistent. When force change is < 0.02 eV Å^{-1}, a geometry optimization is considered convergent. Grimme's DFT-D3 methodology was used to describe the dispersion interactions.

The free energy of a gas phase molecule or an adsorbate on surface was calculated by the equation $G = E + ZPE - TS$, where ZPE is the zero-point energy, T is the temperature in kelvin (298.15 K here), E is the total energy, and S is the entropy. The transition states for elementary reaction steps were determined by combination of the nudged elastic band (NEB) method and the dimer method.[5] As for NEB, the pathway between the reactant and product is discretized to a series of structural images. Then, the image that is closest to a likely transition state structure is applied as an initial guess structure for the dimer method.
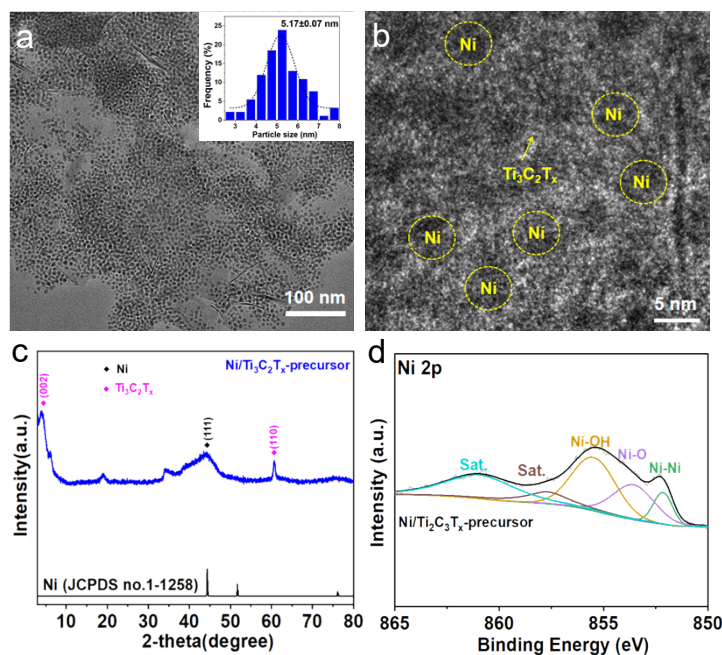
6. Figures and tables
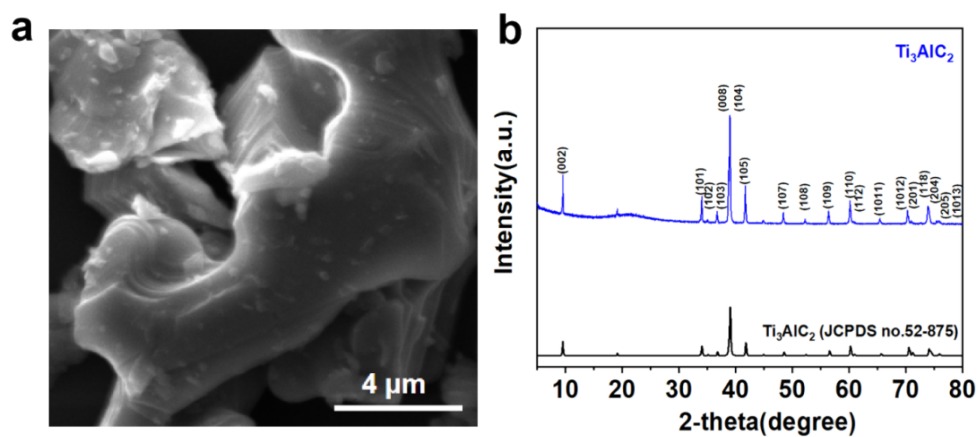
**Fig. S1.** Characterizations of Ti_3AlC_2 MAX phase. (a) SEM image. (b) XRD patterns.
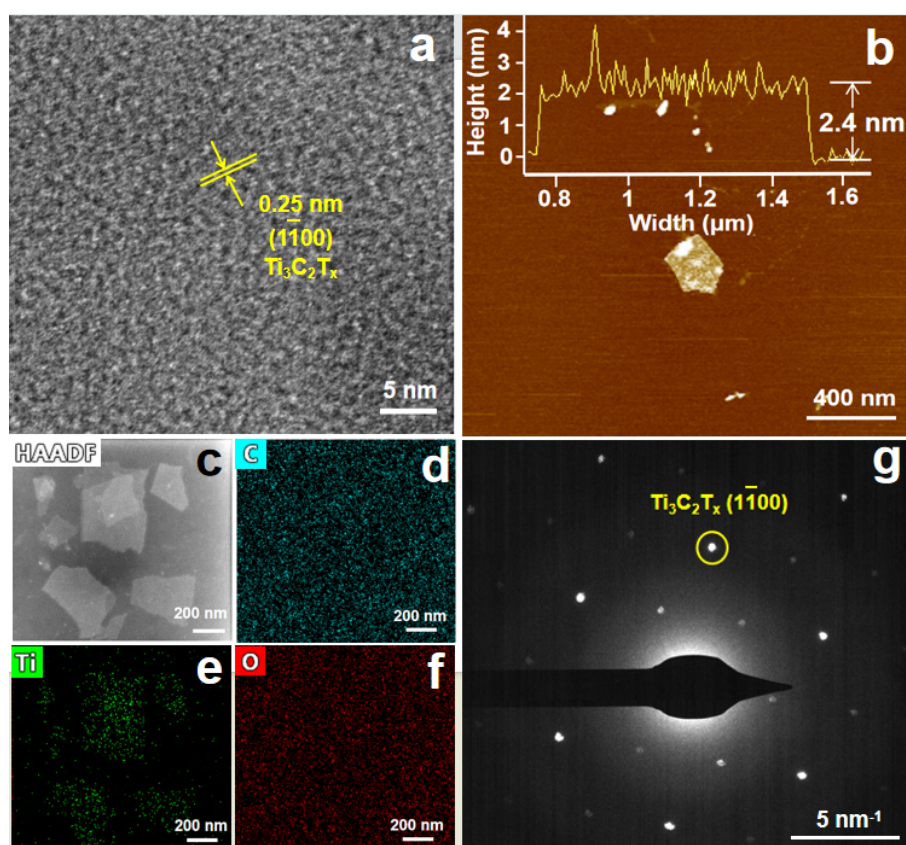
Fig. S2. Characterizations of $Ti_3C_2T_x$ MXene. (a) HRTEM image. (b) AFM image. (c-f) TEM-EDX elemental mapping. (g) SAED pattern.
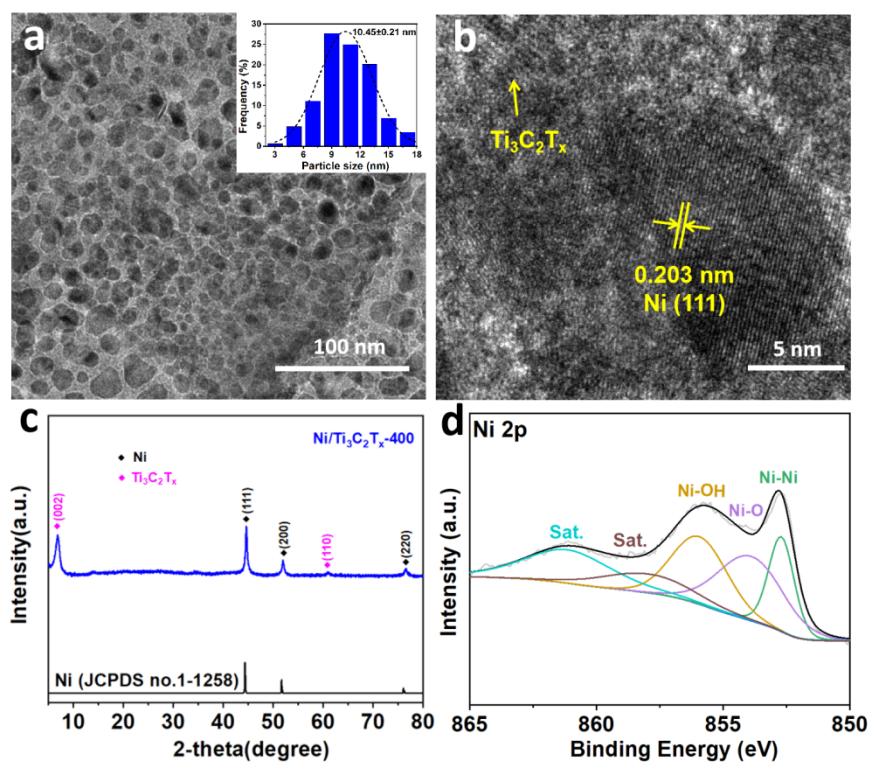
Fig. S3. Characterizations of Ni/Ti$_3$C$_2$T$_x$-precursor. (a) TEM images. Inset of (a) shows the distribution histogram of particle size. (b) HRTEM image. (c) XRD pattern. (d) High-resolution XPS spectrum of Ni 2p.
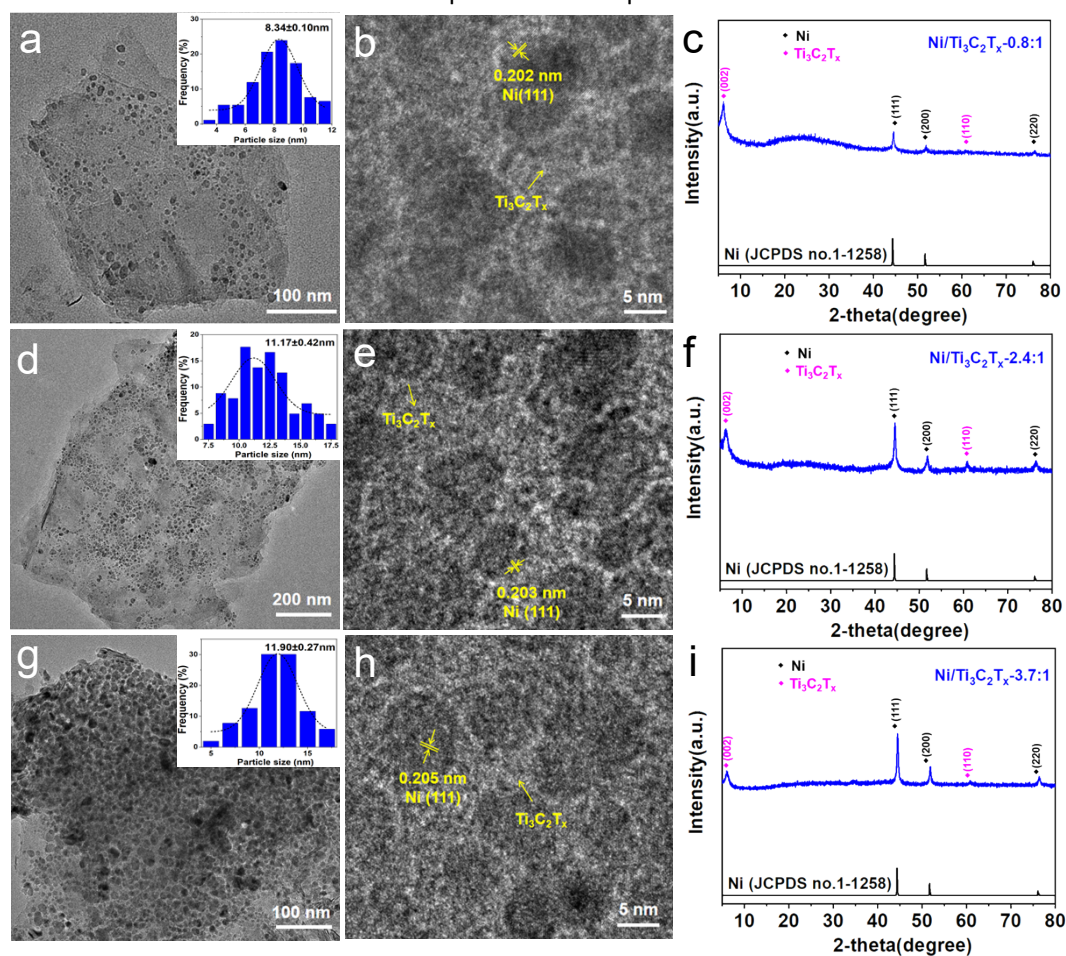
Fig. S4. Characterizations of Ni/Ti$_3$C$_2$T$_x$ with different Ni:Ti$_3$C$_2$T$_x$ mass ratios. (a, d, g) TEM images. Inset of (a, d, g) shows the distribution histogram of particle size. (b, e, h) HRTEM images. (c, f, i) XRD patterns. Different mass ratios of Ni:Ti$_3$C$_2$T$_x$ were achieved by changing the addition amount of Ni(acac)$_2$ and measured by ICP-AES.
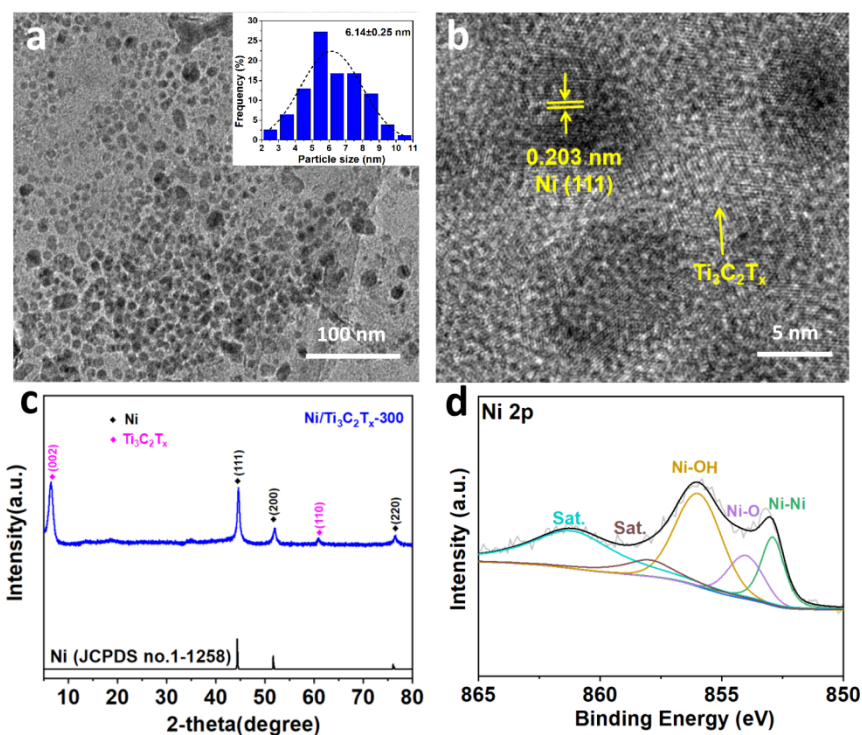
Fig. S5. Characterizations of Ni/Ti$_3$C$_2$T$_x$-300. (a) TEM images. Inset of (a) shows the distribution histogram of particle size. (b) HRTEM image. (c) XRD pattern. (d) High-resolution XPS spectrum of Ni 2p.
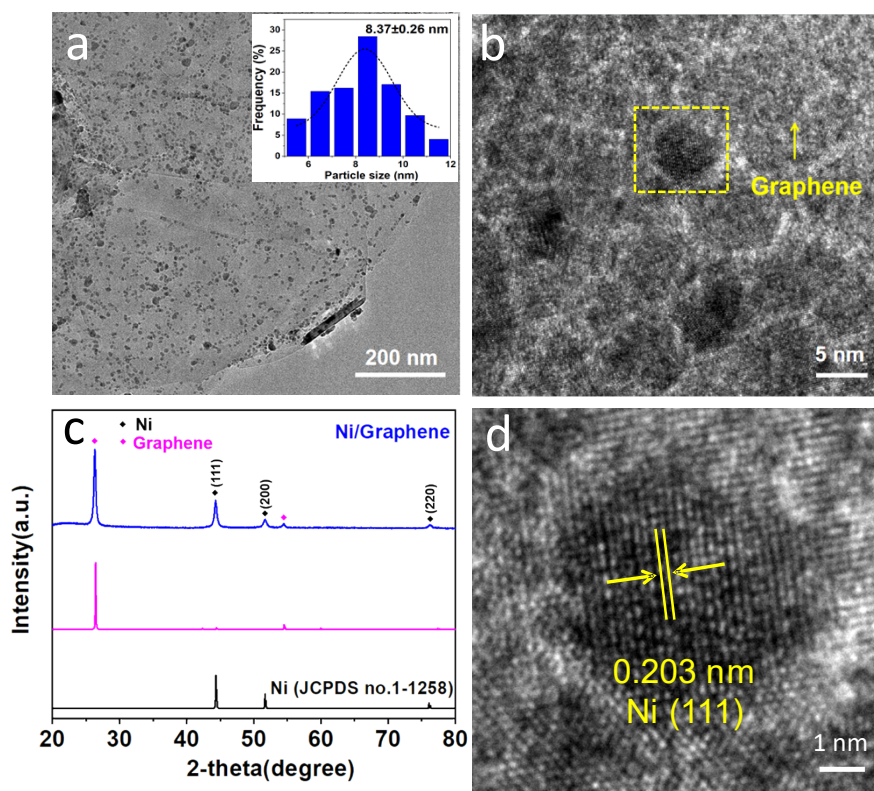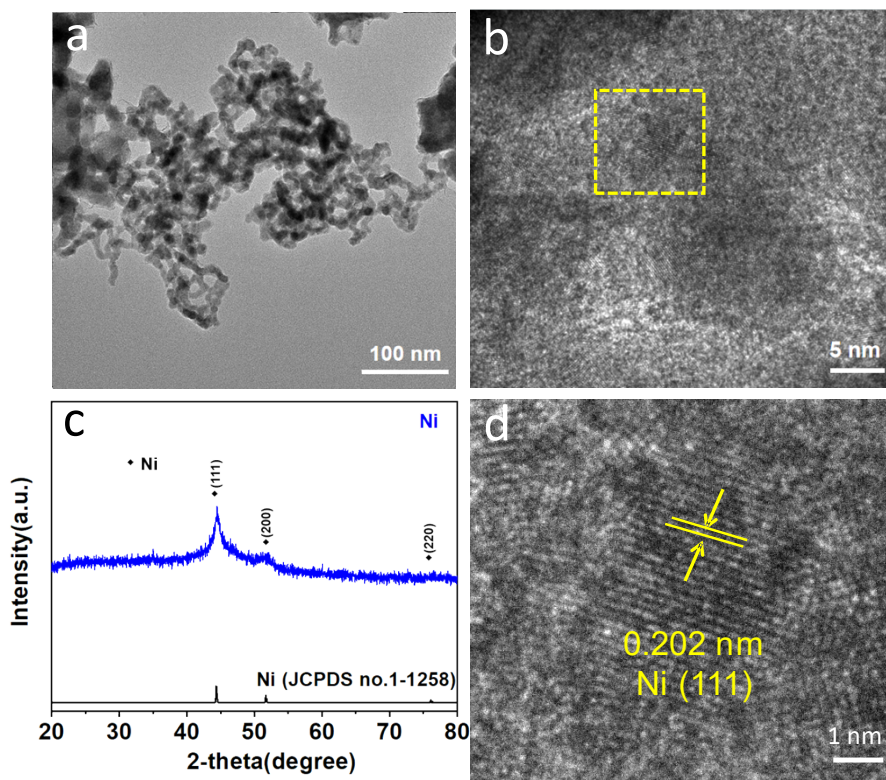

Fig. S6. Characterizations of Ni/Ti$_3$C$_2$T$_x$-400. (a) TEM images. Inset of (a) shows the distribution histogram of particle size. (b) HRTEM image. (c) XRD pattern. (d) High-resolution XPS spectrum of Ni 2p.
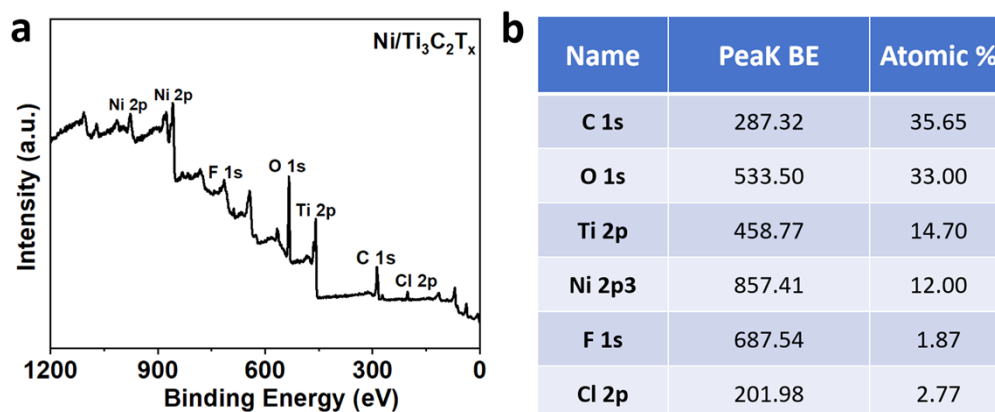
Fig. S7. Characterizations of Ni/G. (a) TEM images. Inset of (a) shows the distribution histogram of particle size. (b) HRTEM image. (c) XRD pattern. (d) Enlarged image inside the yellow dashed box of Fig. S7b.
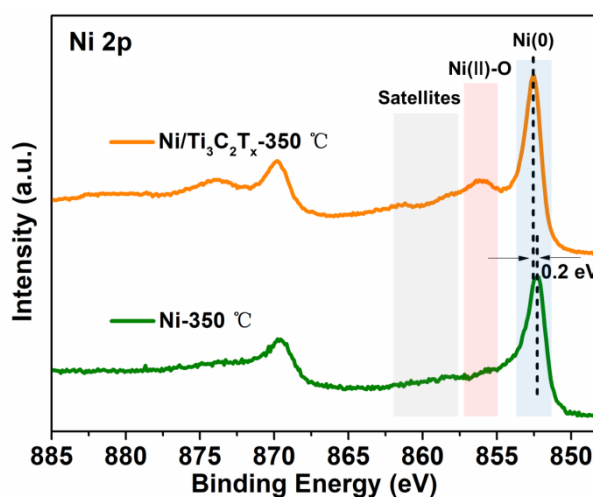

Fig. S8. Characterizations of Ni. (a) TEM image. (b) HRTEM image. (c) XRD pattern. (d) Enlarged image inside the yellow dashed box of Fig. S8b.

a Ni/Ti$_3$C$_2$T$_x$

Intensity (a.u.)

Ni 2p Ni 2p

F 1s O 1s

Ti 2p

C 1s Cl 2p

Binding Energy (eV)

b

Name	PeaK BE	Atomic %
C 1s	287.32	35.65
O 1s	533.50	33.00
Ti 2p	458.77	14.70
Ni 2p3	857.41	12.00
F 1s	687.54	1.87
Cl 2p	201.98	2.77

Fig. S9. Characterizations of Ni/Ti$_3$C$_2$T$_x$. (a) XPS survey spectrum. (b)Element ratio obtained from the XPS test.

Bond	Ni/Ti$_3$C$_2$T$_x$	Ni/G	Ni	Ni/Ti$_3$C$_2$T$_x$-300	Ni/Ti$_3$C$_2$T$_x$-400	Ni/Ti$_3$C$_2$T$_x$-precursor
Ni-Ni	0.25	0.29	0.47	0.2	0.24	0.14
Ni-O	0.25	0.13	0.17	0.29	0.40	0.34
Ni-OH	0.50	0.58	0.36	0.51	0.36	0.52

Fig. S10. Chemical bond composition ratios of Ni 2p for Ni/Ti$_3$C$_2$T$_x$, Ni/G, Ni, Ni/Ti$_3$C$_2$T$_x$-300, Ni/Ti$_3$C$_2$T$_x$-400 and Ni/Ti$_3$C$_2$T$_x$-precursor.

Ni 2p

Ni(0)
Ni(II)-O
Satellites

Ni/Ti$_3$C$_2$T$_x$-350 ℃
Ni-350 ℃

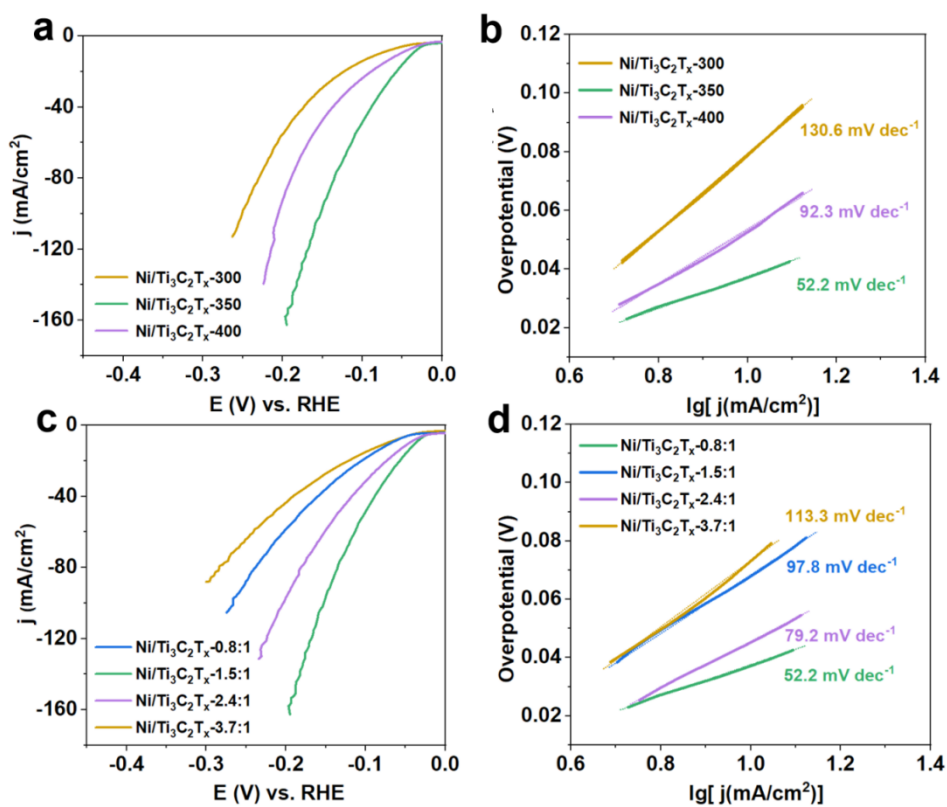0.2 eV

Intensity (a.u.)

Binding Energy (eV)

Fig. S11. In situ XPS of the Ni 2p region of Ni/Ti$_3$C$_2$T$_x$ and pure Ni sintered at 350 °C for 2 h in an atmosphere of H$_2$/Ar=1:9.
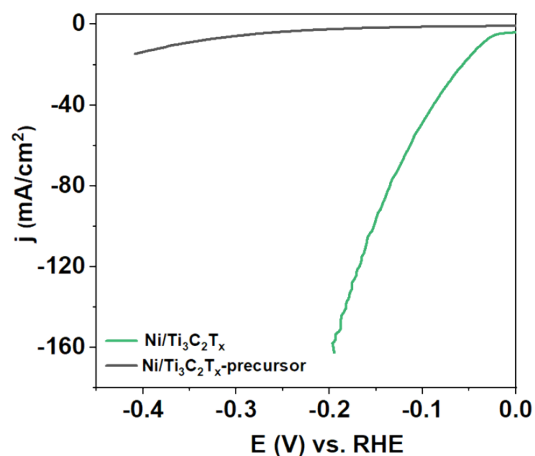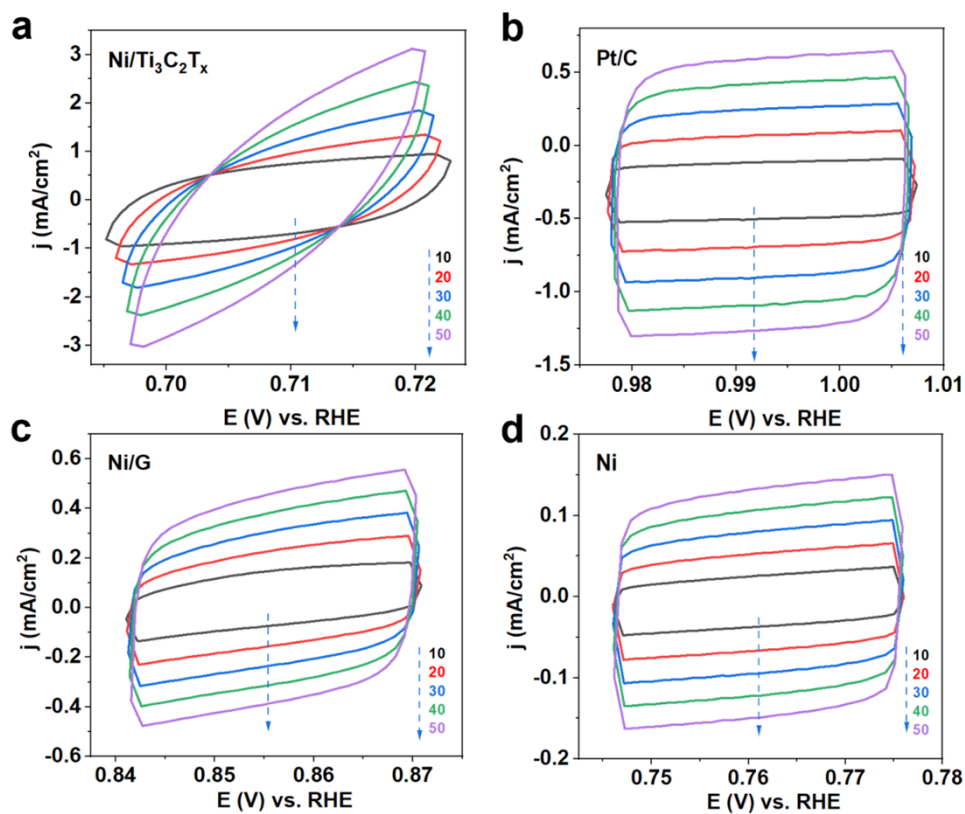
Fig. S12. Polarization curves of Ni/Ti$_3$C$_2$T$_x$ and Ni/Ti$_3$C$_2$T$_x$-precursor for HER. Sweep rate: 5 mV s^{-1}. Rotation speed: 2000 rpm.

Fig. S13. (a) Polarization curves and (b) Tafel slopes Ni/Ti$_3$C$_2$T$_x$ sintered at different temperatures. (c) Polarization curves and (d) Tafel slopes with different mass ratios of Ni:Ti$_3$C$_2$T$_x$. Sweep rate: 5 mV s^{-1}. Rotation speed: 2000 rpm.

Fig. S14. Double-layer capacitance (C_{dl}) measurements in 1 M KOH. CV curves at different scan rates within the non-Faradaic potential range for (a) Ni/Ti$_3$C$_2$T$_x$. (b) Pt/C. (c) Ni/G. (d) Ni.
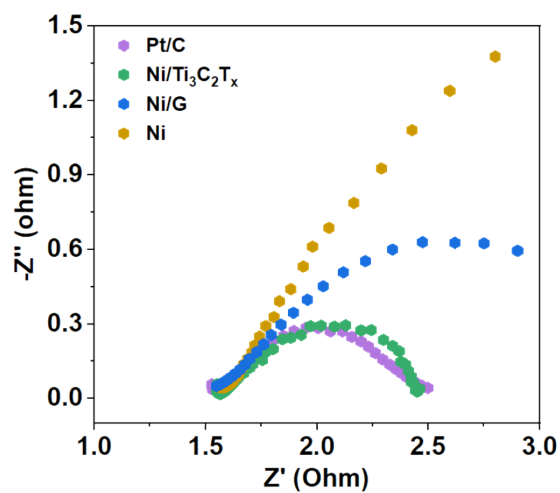
Fig. S15. Electrochemical impedance spectroscopy (EIS) of Pt/C, Ni/Ti$_3$C$_2$T$_x$, Ni/G and Ni.
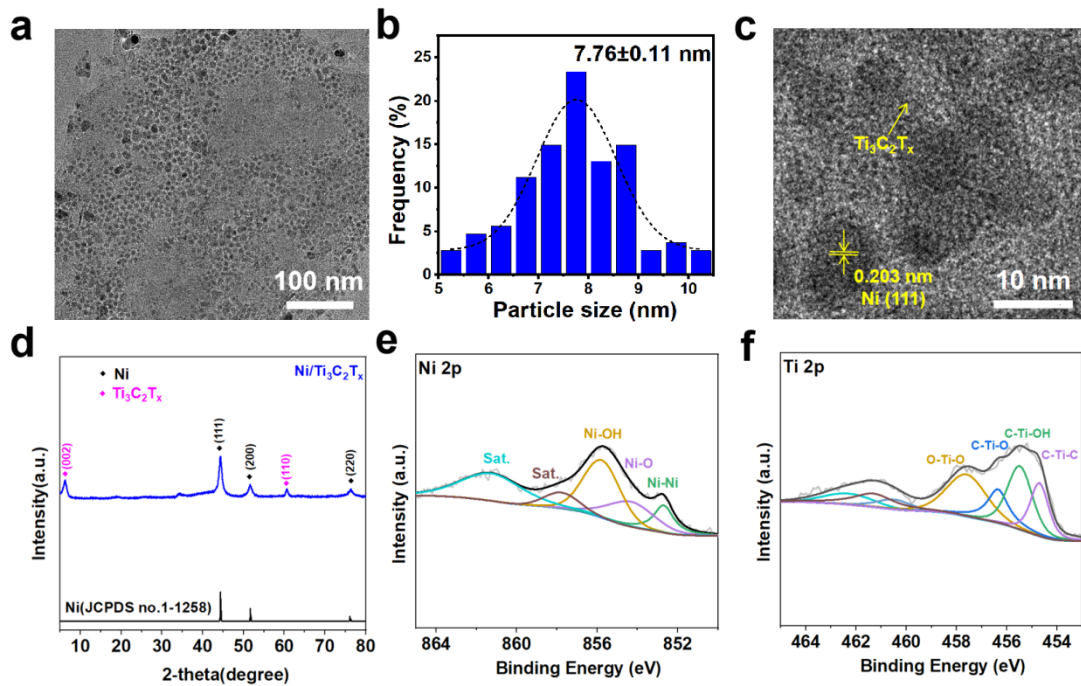
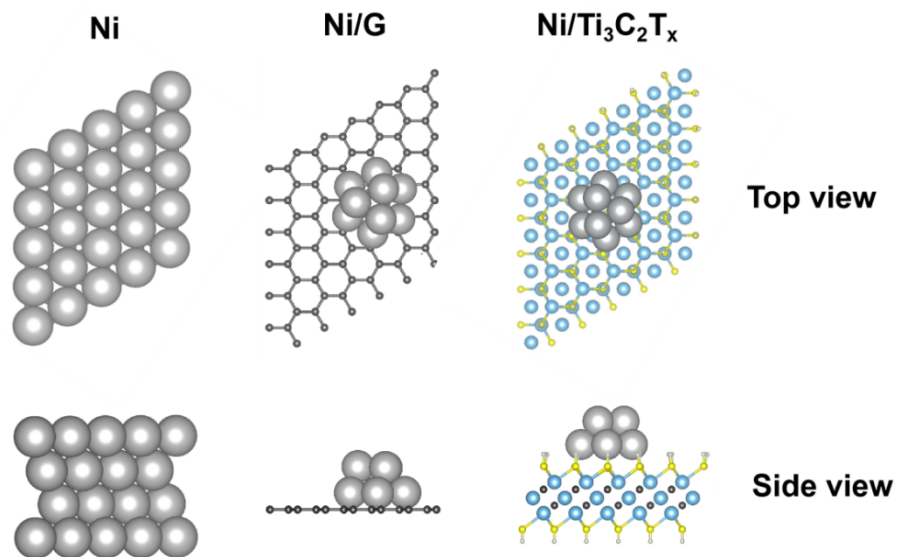**Fig. S16.** The characterizations of Ni/Ti$_3$C$_2$T$_x$ after HER test. (a) TEM image of Ni/Ti$_3$C$_2$T$_x$ after HER test. (b) The size distribution histogram of Ni nanoparticles after HER test. (c) High-resolution TEM images of Ni/Ti$_3$C$_2$T$_x$ after HER test. (d) XRD pattern of Ni/Ti$_3$C$_2$T$_x$ after HER test. (e) Ni 2p XPS spectra and (f) Ti 2p XPS spectra of Ni/Ti$_3$C$_2$T$_x$ after HER test.

Fig. S17. Atomic configurations of Ni, Ni/G and Ni/Ti$_3$C$_2$T$_x$. (blue, dark grey, yellow, light green, and light grey colored balls represent Ti, C, O, H, and Ni atoms, respectively).

Ni   **Ni/G**

Top view

Side view
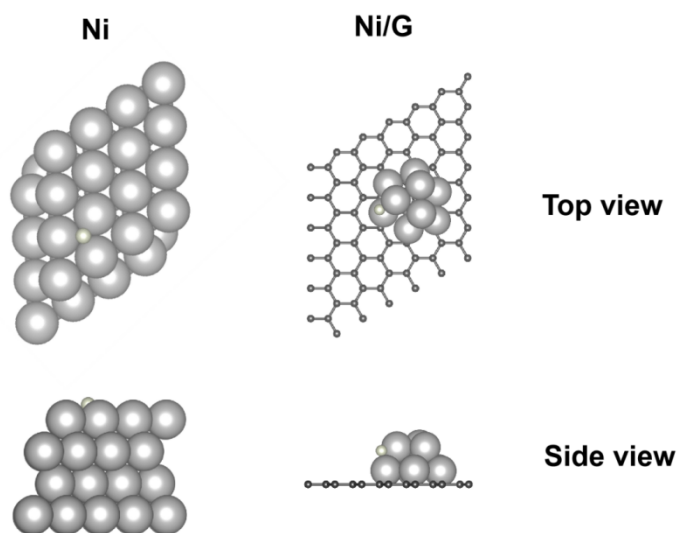
Fig. S18. Adsorption configurations of H* on Ni and Ni/G.
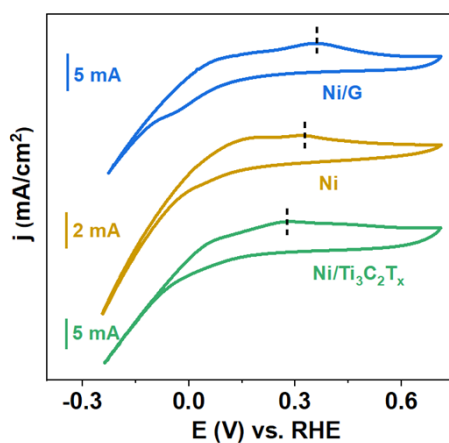
Fig. S19. OH adsorption/desorption on Ni/Ti$_3$C$_2$T$_x$, Ni/G and Ni surfaces.

*H$_2$O   **TS**   ***OH+*H**

Top view

Side view
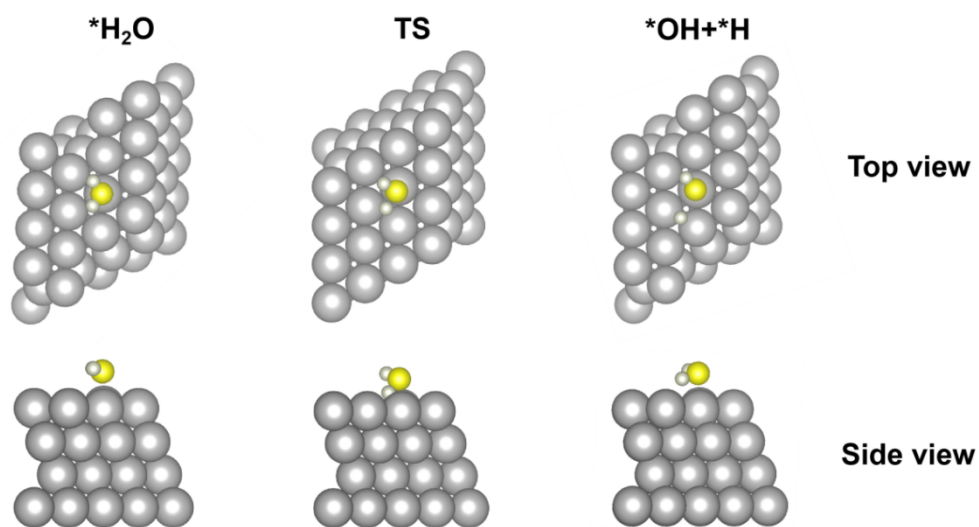
Fig. S20. Atomic configurations of water dissociation process on Ni.
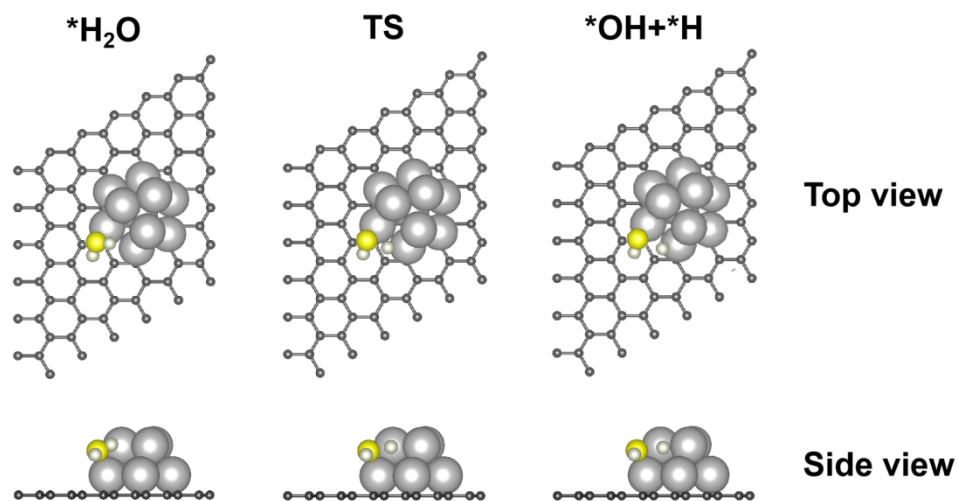
Fig. S21. Atomic configurations of water dissociation process on Ni/G.

Table 1. Compositions of Ni:$Ti_3C_2T_x$ determined by ICP-AES

Sample	Ni:$Ti_3C_2T_x$ mass ratios
Ni/$Ti_3C_2T_x$-0.8:1	0.8:1
Ni/$Ti_3C_2T_x$-1.5:1	1.5:1
Ni/$Ti_3C_2T_x$-2.4:1	2.4:1
Ni/$Ti_3C_2T_x$-3.7:1	3.7:1

Table 2. Comparison of the electrocatalytic activity of Ni/$Ti_3C_2T_x$ in 1.0 M KOH electrolyte with reported catalysts for HER.

Catalyst	Overpotential (mV) at 10 mA cm^{-2}	Tafel slope (mV dec^{-1})
Ni/$Ti_3C_2T_x$[this work]	36	52.2
Ni/G[this work]	126	143
Ni[this work]	205	184.5
$MoNi_4$/MoO_2@Ni[6]	15	30
Pt/CuO[7]	39	41.7
PtNi-O[8]	39.8	78.8
Ru-G/CC[9]	40	76
a-Ru@Co-DHC[10]	40	62

CoP-CeO$_2$/Ti[11]	43	45
Ru-NiFe-P[12]	44	80
Ni NCNA[13]	47	41
CF/Ni$_3$N/VON[14]	48	45
Ni(OH)$_2$/Ni$_3$S$_2$[15]	50	49
Ru/C-H$_2$O/CH$_3$CH$_2$OH[16]	53	47
Ni–P/Ni(OH)$_2$[17]	54.7	58
MoS$_2$/Ni$_3$S$_2$ NRs[18]	56	82
Ni/β-Ni(OH)[19]	58	78.1
Ni$_2$P-NiSe$_2$[20]	66	72.6
Ni-Ni(OH)$_2$[21]	72	43
V-Ce/CoFe LDH[22]	73	69
S-MoP/CC[23]	75	59.1
Mn–Co–P/Ti[24]	76	52
Co–MoC/Mo$_2$C[25]	82	54
Ni/TiO$_2$ NPAs[26]	88	78
NMCP@NF[27]	88	70
Ni/Fe$_3$C[28]	93	63
NCNT-NP@NF[29]	96.1	84.8
O-CoMoS[30]	97	70
SC-FeNiCeP/NF[31]	107	41.54
WSe$_2$ SSC[32]	115	97
SA-Pt/MoS$_2$[33]	123	76.71
PdSe$_2$[34]	138	100
Ni–N–C[35]	147	114

References

1   F. l. Yang, P. Y. Han, N. Yao, G. Z. Cheng, S. L. Chen, W. Luo, Inter-regulated d-band centers of the Ni_3B/Ni heterostructure for boosting hydrogen electrooxidation in alkaline media, Chem. Sci., 2020, **11**, 12118-12123.

2   G. Kresse, J. Furthmüller, Efficient iterative schemes for ab initio total-energy calculations using a plane-wave basis set, Phys. Rev. B., 1996, **54**, 11169.

3   B. Hammer, L. B. Hansen, J. K. Nørskov, Improved adsorption energetics within density-functional theory using revised Perdew-Burke-Ernzerhof functionals, Phys. Rev. B., 1999, **59**, 7413-7421.

4   P. E. Blöchl, Projector augmented-wave method, Phys. Rev. B., 1994, **50**, 17953-17979.

5   G. Henkelman, B. P. Uberuaga, H. Jónsson, A climbing image nudged elastic band method for finding saddle points and minimum energy paths, J. Chem. Phys., 2000, **113**, 9901-9904.

6   J. Zhang, T. Wang, P. Liu, Z. Q. Liao, S. H. Liu, X. D. Zhuang, M. W. Chen, E. Zschech, X. L. Feng, Efficient hydrogen production on $MoNi_4$ electrocatalysts with fast water dissociation kinetics, Nat. Commun., 2017, **8**, 15437.

7   P. J. Wang, Y. T. Yan, P. C. Wang, Z. Y. Ye, X. H. Zheng, W. Cai, Highly dispersed Pt/CuO nanoclusters in N-doped porous carbon array for superior hydrogen evolution, Chem. Eng. J., 2023, **455**, 140856.

8   Z. P. Zhao, H. T. Liu, W. P. Gao, W. Xue, Z. Y. Liu, J. Huang, X. Q. Pan, Y. Huang, Surface-Engineered PtNi-O Nanostructure with Record-High Performance for Electrocatalytic Hydrogen Evolution Reaction, J. Am. Chem. Soc., 2018, **140**, 9046-9050.

9   M. Z. You, X. Du, X. H. Hou, Z. Y. Wang, Y. Zhou, H. P. Ji, L. Y. Zhang, Z. T. Zhang, S. S. Yi, D. L. Chen, In-situ growth of ruthenium-based nanostructure on carbon cloth for superior electrocatalytic activity towards HER and OER, Appl. Catal. B Environ., 2022, **317**, 121729.

10   W. X. Yang, W. Y. Zhang, R. Liu, F. Lv, Y. G. Chao, Z. C. Wang, S. J. Guo, Amorphous Ru nanoclusters onto Co-doped 1D carbon nanocages enables efficient hydrogen evolution catalysis, Chin. J. Catal., 2022, **43**, 110-115.

11   R. Zhang, X. Ren, S. Hao, R. X. Ge, Z. A. Liu, A. M. Asiri, L. Chen, Q. J. Zhang, X. Q. Sun, Selective phosphidation: an effective strategy toward CoP/CeO_2 interface engineering for superior alkaline hydrogen evolution electrocatalysis, J. Mater. Chem. A., 2018, **6**, 1985-1990.

12   M. J. Qu, Y. M. Jiang, M. Yang, S. Liu, Q. F. Guo, W. Shen, M. Li, R. X. He, Regulating electron density of NiFe-P nanosheets electrocatalysts by a trifle of Ru for high-efficient overall water splitting, Appl. Catal. B Environ., 2020, **263**, 118324.

13   Y. P. Li, J. M. Li, Q. Z. Qian, X. Jin, Y. Liu, Z. Y. Li, Y. Zhu, Y. M. Guo, G. Q. Zhang, Superhydrophilic Ni-based Multicomponent Nanorod-Confined-Nanoflake Array Electrode Achieves Waste-Battery-Driven Hydrogen Evolution and Hydrazine Oxidation, Small., 2021, **17**, 2008148.

14   T. Z. Xiong, J. T. Li, J. C. Roy, M. Koroma, Z. X. Zhu, H. Yang, L. Zhang, T. Ouyang, M. S. Balogun, M. A. Mamun, Hetero-interfacial nickel nitride/vanadium oxynitride porous nanosheets as trifunctional electrodes for HER, OER and sodium ion batteries, J. Energy Chem., 2023, **81**, 71-81.

15   Q. C. Xu, H. Jiang, H. X. Zhang, Y. J. Hu, C. Z. Li, Heterogeneous interface engineered atomic configuration on ultrathin $Ni(OH)_2/Ni_3S_2$ nanoforests for efficient water splitting, Appl. Catal. B Environ., 2019, **242**, 60-66.

16   Y. Z. Li, J. Abbott, Y. C. Sun, J. M. Sun, Y. C. Du, X. J. Han, G. Wu, P. Xu, Ru nanoassembly

catalysts for hydrogen evolution and oxidation reactions in electrolytes at various pH values, Appl. Catal. B Environ., 2019, **258**, 117952.

17   F. Z. Zhao, H. C. Liu, H. Y. Zhu, X. Y. Jiang, L. Q. Zhu, W. P. Li, H. N. Chen, Amorphous/amorphous Ni–P/Ni(OH)$_2$ heterostructure nanotubes for an efficient alkaline hydrogen evolution reaction, J. Mater. Chem. A., 2021, **9**, 10169-10179.

18   Y. Zhao, S. Z. Wei, L. B. Xia, K. M. Pan, B. Zhang, H. Huang, Z. L. Dong, H. H. Wu, J. P. Lin, H. Pang, Sintered Ni metal as a matrix of robust self-supporting electrode for ultra-stable hydrogen evolution, Chem. Eng. J., 2022, **430**, 133040.

19   D. Shao, Q. Wang, X. Z. Yao, Y. T. Zhou, X. Y. Yu, Phase-engineering of nickel hydroxide in the Ni/Ni(OH)$_2$ interface for efficient hydrogen evolution and hydrazine-assisted water splitting in seawater, J. Mater. Chem. A., 2022, **10**, 21848-21855.

20   C. C. Liu, T. Gong, J. Zhang, X. R. Zheng, J. Mao, H. Liu, Y. Li, Q. Y. Hao, Engineering Ni$_2$P-NiSe$_2$ heterostructure interface for highly efficient alkaline hydrogen evolution, Appl. Catal. B Environ., 2020, **262**, 118245.

21   W. D. Zhong, W. L. Li, C. F. Yang, J. Wu, R. Zhao, M. Idrees, H. Xiang, Q. Zhang, X. K. Li, Interfacial electron rearrangement: Ni activated Ni(OH)$_2$ for efficient hydrogen evolution, J. Energy Chem., 2021, **61**, 236-242.

22   S. J. Liu, J. Zhu, M. Sun, Z. X. Ma, K. Hu,T. Nakajima, X. H. Liu, P. Schmuki, L. Wang, Promoting the hydrogen evolution reaction through oxygen vacancies and phase transformation engineering on layered double hydroxide nanosheets, J. Mater. Chem. A., 2020, **8**, 2490-2497.

23   M. H. Hu, B. C. Liu, H. Y. Chen, X. Xu, P. Jing, X. L. Guo, R. Yang, X. Y. Wang, R. Gao, J. Zhang, Universal construction of sulfur doped molybdenum-based nanosheets for enhanced hydrogen evolution in a wide pH range, Appl. Catal. B Environ., 2023, **322**, 122131.

24   T. T. Liu, X. Ma, D. N. Liu, S. Hao, G. Du, Y. J. Ma, A. M. Asiri, X. P. Sun, L. Chen, Mn Doping of CoP Nanosheets Array: An Efficient Electrocatalyst for Hydrogen Evolution Reaction with Enhanced Activity at All pH Values, ACS Catal., 2017, **7**, 98-102.

25   J. C. Li, R. Y. Ge, P. P. Lan, J. Yang, J. Feng, Y. Li, S. Li, B. Liu, W. X. Li, In situ phase transition induced TM–MoC/Mo$_2$C (TM= Fe, Co, Ni, and Cu) heterostructure catalysts for efficient hydrogen evolution, J. Mater. Chem. A., 2022, **10**, 10493-10502.

26   Y. Li, K. A. Min, B. C. Han, L. Y. S. Lee, Ni nanoparticles on active (001) facet-exposed rutile TiO$_2$ nanopyramid arrays for efficient hydrogen evolution, Appl. Catal. B Environ., 2021, **282**, 119548.

27   M. R. Kandel, U. N. Pan, D. R. Paudel, P. P. Dhakal, N. H. Kim, J. H. Lee, Hybridized bimetallic phosphides of Ni–Mo, Co–Mo, and Co–Ni in a single ultrathin-3D-nanosheets for efficient HER and OER in alkaline media, Compos B Eng., 2022, **239**, 109992.

28   C. F. Yang, R. Zhao, H. Xiang, J. Wu, W. D. Zhong, W. L. Li, Q. Zhang, N. J. Yang, X. K. Li, Ni-Activated Transition Metal Carbides for Efficient Hydrogen Evolution in Acidic and Alkaline Solutions, Adv. Energy Mater., 2020, **10**, 2002260.

29   Y. Cheng, H. R. Guo, P. F. Yuan, X. P. Li, L. R. Zheng, R. Song, Self-supported bifunctional electrocatalysts with Ni nanoparticles encapsulated in vertical N-doped carbon nanotube for efficient overall water splitting, Chem. Eng. J., 2021, **413**, 127531.

30   J. G. Hou, B. Zhang, Z. W. Li, S. Y. Cao, Y. Q. Sun, Y. Z. Wu, Z. M. Gao, L. C. Sun, Vertically Aligned Oxygenated-CoS$_2$–MoS$_2$ Heteronanosheet Architecture from Polyoxometalate for Efficient and Stable Overall Water Splitting, ACS Catal., 2018, **8**, 4612-4621.

31   Q. Q. Wang, X. Y. Ma, W. You, P. C. Ma, R. Bi, S. Y. Song, F. Chen, F. J. Qu, X. L. Wang, P. F. Liu,

High-valence metal engineered trimetallic organic framework derived S, C co-doped FeNiCeP nanospheres for proficient self-powered overall water splitting, Chem. Eng. J., 2024, **482**, 148712.

32   P. Pazhamalai, K. Krishnamoorthy, R. Swaminathan, V. Natraj, S. J. Kim, Unravelling the trifunctional electrochemical properties of WSe_2 nanosheets for self-powered hydrogen production, Nano Energy., 2024, **120**, 109084.

33   J. T. Zhu, Y. D. Tu, L. J. Cai, H. B. Ma, Y. Chai, L. F. Zhang, W. J. Zhang, Defect-Assisted Anchoring of Pt Single Atoms on MoS_2 Nanosheets Produces High-Performance Catalyst for Industrial Hydrogen Evolution Reaction, Small., 2022, **18**, 2104824.

34   Z. P. Lin, B. B. Xiao, Z. P. Wang, W. Y. Tao, S. J. Shen, L. G. Huang, J. T. Zhang, F. Q. Meng, Q. H. Zhang, L. Gu, W. W. Zhong, Planar-Coordination $PdSe_2$ Nanosheets as Highly Active Electrocatalyst for Hydrogen Evolution Reaction, Adv. Funct. Mater., 2021, **31**, 2102321.

35   C. J. Lei, Y. Wang, Y. Hou, P. Liu, J. Yang, T. Zhang, X. D. Zhuang, M. W. Chen, B. Yang, L. C. Lei, C. Yuan, M. Qiu, X. L. Feng, Efficient alkaline hydrogen evolution on atomically dispersed Ni–N_x Species anchored porous carbon with embedded Ni nanoparticles by accelerating water dissociation kinetics, Energy Environ. Sci., 2019, **12**,149-156.